Modeling the Bifilar Pendulum Using Nonlinear, Flexible Multibody Dynamics

Olivier A. Bauchau Jesus Rodriguez Shyi-Yaung Chen
School of Aerospace Engineering
Georgia Institute of Technology, Atlanta, GA
Research and Engineering
Sikorsky Aircraft, Stratford, CT

This paper deals with the modeling of the bifilar pendulum, a hub-mounted self-tuning vibration absorber used on certain rotorcraft. The bifilar consists of a tuning mass that acts as a pendulum and is connected to a support frame by means of two cylindrical tuning pins. The tuning pins roll without sliding on curves of cycloidal shape machined into the tracking holes on the support frame and tuning mass. In this work, a detailed model of this device is presented, which involves nonlinear holonomic and nonholonomic constraints. The formulation is developed within the framework of finite element based dynamic analysis of nonlinear, flexible multibody systems, and features energy preserving and decaying time integration schemes that provide unconditional stability for nonlinear systems. Numerical examples are presented that demonstrate the efficiency and accuracy of the proposed approach.

Introduction

The bifilar pendulum is a self-tuning vibration alleviation device mounted on the main rotor hub of rotorcraft, and its basic components are shown in Fig. 1. A main tuning mass is attached to a support arm by means of two pins rolling on the tracking holes. Experimental evidence, such as wear patterns on the tracking holes, indicates that the circular pins are in rolling contact with the support arm and the tuning mass at all times. The natural frequency of the system is tuned so as to absorb in-plane rotor vibrations at a specified frequency. The bifilar pendulum has a long history: Den Hartog (Ref. 1) credits Sarazin in France and Chilton in the United States with the independent invention of the bifilar pendulum as a vibration absorber in multicylinder engines. A description of several configurations of rotorhead absorbers is found in Refs. 2–4.

The goal of this paper is to develop a detailed and accurate model of this device within the framework of multibody system dynamics (Refs. 5–7). In this approach, complex dynamical systems are represented as a collection of rigid or flexible bodies connected by joints. In view of their solid steel construction, the tuning mass and support arm of the bifilar pendulum can be considered to be rigid bodies. The challenge of this work is to model the kinematic conditions associated with the rolling of the tuning pins on the tracking holes by means of a set of joints that impose the proper kinematic constraints between these two bodies. It will be assumed that the pin remains in rolling contact with the tracking holes at all times, as suggested by experimental evidence.

The topics of contact, intermittent contact, and impact have received considerable attention in the multibody dynamics literature. When analyzing a system involving contact, the kinematics of the problem are expressed in terms of candidate contact points (Ref. 8), i.e., the points of the bodies that are the most likely to come in contact. The candidate contact points are determined by a number of nonlinear holonomic constraints that involve the kinematic variables defining the configuration of the contacting bodies and the parameters that describe the curve representing their outer shape. The knowledge of the location of these candidate contact points leads to the definition of the relative distance q between the bodies. This approach was used by a number of researchers such as Khulief and Shabana (Ref. 9), Lankarani and Nikravesh (Ref. 10), Cardona and Géradin (Ref. 11), and Bauchau et al. (Refs. 12–15) among others.

Although directly applicable to modeling of the bifilar pendulum, these various approaches are unnecessarily complex. If intermittent contact can occur, the relative distance q between the bodies must be evaluated at each time step during the simulation and the conditions for contact or separation must be checked as well. Under the assumption of continuous rolling contact, the relative distance vanishes at all times, resulting in considerably simpler formulations.

The kinematic conditions associated with the sliding of a body along a flexible track have been presented by Li and Likins (Ref. 16) within the framework of Kane's method. Cardona (Ref. 17) derived a finite element based formulation for the sliding of a body along a prescribed curve. Finally, Bauchau (Ref. 18) presented the formulation of a sliding joint that enforces the sliding of a body along a flexible beam. This formulation was later refined (Ref. 19) to include constraints on the relative rotation between the sliding bodies. These formulations could form the basis for modeling the bifilar pendulum, but are again of unnecessary complexity. Indeed, the flexibility of the tracking holes has most likely negligible effect. The formulation proposed in this work relies on a curve sliding joint that enforces the sliding of a body on a rigid curve connected to another body.

The paper is organized in the following manner. After a brief definition of the notational conventions used in this paper, the concept of joints in multibody systems is briefly discussed. Next, the modeling of a bifilar pendulum with circular tracking holes is presented, and the formulation is then extended to account for tracking holes of arbitrary shape. The proposed model makes extensive use of a curve sliding joint, the

Manuscript received February 2002; accepted November 2002.

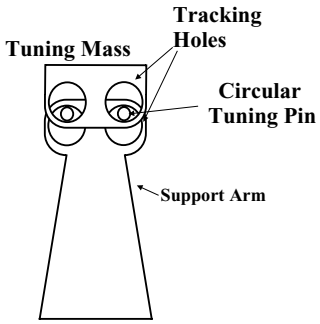

Fig. 1. The bifilar pendulum.

formulation of which is detailed in the next section. Finally, numerical examples are presented to validate the proposed formulation. The paper concludes with the presentation of a model of the UH-60 rotor system that includes the four hub-mounted bifilar pendulums.

Notational Conventions

The kinematic description of bodies in their reference and deformed configurations will make use of three orthonormal bases. First, an inertial basis is used as a global reference for the system; it is denoted $\mathcal{S}^I := (\mathbf{i}_1, \mathbf{i}_2, \mathbf{i}_3)$. A second basis $\mathcal{S}^0 := (\mathbf{e}_{01}, \mathbf{e}_{02}, \mathbf{e}_{03})$, is attached to the body and defines its orientation in the reference configuration. Finally, a third basis $\mathcal{S} := (\mathbf{e}_1, \mathbf{e}_2, \mathbf{e}_3)$ defines the orientation of the body in its deformed configuration.

Let $\mathbf{u}_0$ and $\mathbf{u}$ be the displacement vectors from $\mathcal{S}^I$ to $\mathcal{S}^0$, and $\mathcal{S}^0$ to $\mathcal{S}$, respectively, and $\mathbf{R}_0$ and $\mathbf{R}$ the rotation tensors from $\mathcal{S}^I$ to $\mathcal{S}^0$, and $\mathcal{S}^0$ to $\mathcal{S}$, respectively. In this work, all vector and tensor components are measured in either $\mathcal{S}^I$ or $\mathcal{S}$. For instance, the components of vector $\mathbf{u}$ measured in $\mathcal{S}^I$ and $\mathcal{S}$ will be denoted $\underline{u}$ and $\underline{u}^*$, respectively, and clearly

$$\underline{u}^* = R_0^T R^T \, \underline{u}. \tag{1}$$

Similarly, the components of tensor $\mathbf{R}$ measured in $\mathcal{S}^I$ and $\mathcal{S}$ will be denoted R and R^*, respectively. The skew-symmetric matrix formed with the components $\underline{u}$ will be denoted $\widetilde{u}$.

In this work, the external shape of a rigid body is described by a spatial curve defined by its NURBS (Non-Uniform Rational-B-Spline) representation (Refs. 20, 21). The curve is parameterized with the variable $\eta \in [0, 1]$. The Frenet triad associated with a point on a curve is denoted as $\mathcal{S}' := (\mathbf{t}(\eta), \mathbf{n}(\eta), \mathbf{b}(\eta))$, where vectors $\mathbf{t}(\eta)$, $\mathbf{n}(\eta)$ and $\mathbf{b}(\eta)$, are the curve unit tangent, principal normal and binormal vectors, respectively.

Joints in Multibody Systems

In multibody formulations, complex dynamical systems are represented as a collection of rigid or flexible bodies connected by joints. Joints impose constraints on the relative motion of the various bodies of the system. Most joints used for practical applications can be modeled in terms of the so called *lower pairs* (Ref. 22): the revolute, prismatic, screw, cylindrical, planar and spherical joints, all depicted in Fig. 2. If two bodies are rigidly connected to one another, their six relative motions, three displacements and three rotations, must vanish at the connection point. If one of the lower pair joints connects the two bodies, one or more relative motions will be allowed. For instance, the *revolute joint* allows the relative rotation of two bodies about a specific body-attached axis while the other five relative motions remain constrained.

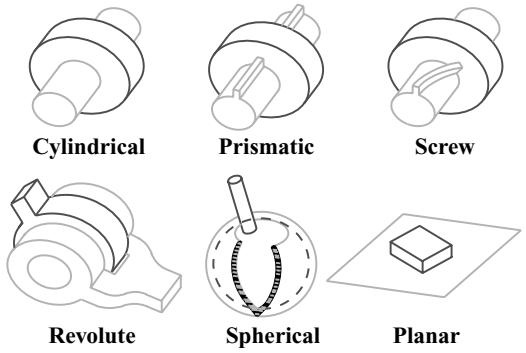

Fig. 2. The six lower pairs.

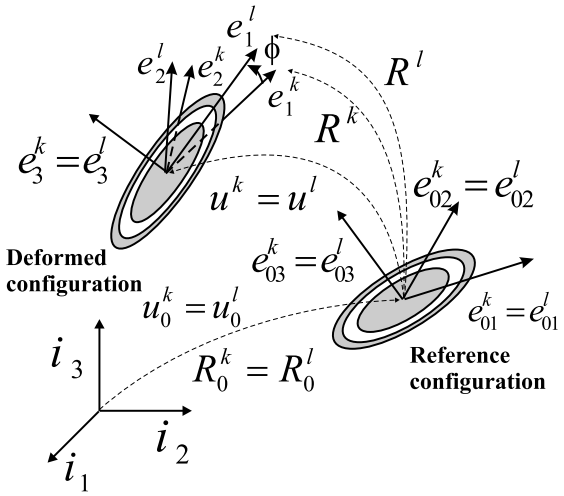

Fig. 3. Revolute joint in the reference and deformed configurations.

The revolute joint

Consider two bodies denoted with superscripts $(.)^k$ and $(.)^\ell$, respectively, linked together by a revolute joint, as depicted in Fig. 3. In the reference configuration, the revolute joint is defined by triads $\mathcal{S}^{0k} := (\mathbf{e}^k_{01}, \mathbf{e}^k_{02}, \mathbf{e}^k_{03})$ and $\mathcal{S}^{0\ell} := (\mathbf{e}^\ell_{01}, \mathbf{e}^\ell_{02}, \mathbf{e}^\ell_{03})$ that are coincident, $\mathcal{S}^{0k} = \mathcal{S}^{0\ell}$. In the deformed configuration, the orientations of the two bodies are defined by two distinct triads, $\mathcal{S}^k := (\mathbf{e}^k_1, \mathbf{e}^k_2, \mathbf{e}^k_3)$ and $\mathcal{S}^\ell := (\mathbf{e}^\ell_1, \mathbf{e}^\ell_2, \mathbf{e}^\ell_3)$. The kinematic constraints associated with a revolute joint imply the vanishing of the relative displacement of the two bodies while the triads $\mathcal{S}^k$ and $\mathcal{S}^\ell$ are allowed to rotate with respect to each other in such a way that $\mathbf{e}^k_3 = \mathbf{e}^\ell_3$. This condition implies the orthogonality of $\mathbf{e}^k_3$ to both $\mathbf{e}^\ell_1$ and $\mathbf{e}^\ell_2$. These two kinematic constraints can be written as

$$\mathcal{C}_1 = \underline{e}^{kT}_3 \, \underline{e}^\ell_1 = 0, \quad \mathcal{C}_2 = \underline{e}^{kT}_3 \, \underline{e}^\ell_2 = 0. \tag{2}$$

In the deformed configuration, the origin of the triads is still coincident. This constraint can be enforced within the framework of finite element formulations by Boolean identification of the corresponding degrees of freedom.

The relative rotation ϕ between the two bodies is defined by adding a third constraint

$$\mathcal{C}_3 = \left(\underline{e}^{kT}_1 \, \underline{e}^\ell_1\right) \sin\phi + \left(\underline{e}^{kT}_1 \, \underline{e}^\ell_2\right) \cos\phi = 0. \tag{3}$$

The three constraints defined by Eqs. (2) and (3) are nonlinear, holonomic constraints that are enforced by the addition of constraint potentials $\lambda_i \, \mathcal{C}_i$,

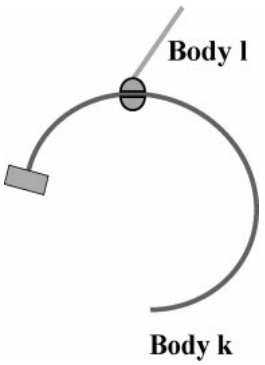

Fig. 4. The curve sliding joint.

where λ_i are the Lagrange multipliers. Details of the formulation of the constraint forces and their discretization can be found in Refs. 23 and 24.

The curve sliding joint

The revolute joint is a very common joint in multibody dynamics. For modeling the bifilar pendulum, a more unusual joint, the *curve sliding joint*, will be necessary. In this joint, depicted in Fig. 4, body ℓ must slide on a curve rigidly connected to body k: a point of body ℓ must be in contact with the curve at all times. This condition will be enforced by a set of nonlinear holonomic constraints. In some cases, the orientation of body ℓ must remain constant with respect to the local Frenet triad associated with of the curve. This is achieved by imposing an additional set of nonlinear holonomic constraints. Details of the formulation of the curve sliding joint will be developed in a later section.

Bifilar with Arbitrarily Shaped Tracking Holes

The kinematic conditions associated with the rolling of the pin on the tracking holes are at the heart of the modeling of the bifilar pendulum. At first, the kinematic constraints corresponding to this configuration are discussed, then the multibody formulation is presented.

Kinematic constraints

Figure 5 shows the configuration of a bifilar pendulum with arbitrary tracking holes. A rotating orthonormal basis $\mathcal{S}^H := (\mathbf{e}_1^H, \mathbf{e}_2^H, \mathbf{e}_3^H)$ is attached at point H to the hub that rotates at an angular speed Ω. The curves defining the shape of the tracking holes are denoted by $\mathbb{C}_1$ and $\mathbb{C}_2$, with curvilinear coordinates denoted s_1 and s_2, respectively. Points O_1 and O_2 are reference points on the support arm and tuning masses, respectively. The center of mass of the tuning mass is located at a distance R_m from point O_2. The circular pin of diameter d is in contact with $\mathbb{C}_1$ and $\mathbb{C}_2$ at points A and B, respectively, and its center is located at point P. Due to the symmetry of the pendulum, see Fig. 1, the tuning mass does not rotate with respect to the hub-attached basis $\mathcal{S}^H$. It is convenient to define the quantities $\underline{\omega}_1^* = -\dot{\theta}\,\underline{e}_3^H$ and $\underline{\omega}_2^* = -\dot{\gamma}\,\underline{e}_3^H$ which are the angular velocities of the pin measured in the Frenet triads associated with curve $\mathbb{C}_1$ at the point of contact A and $\mathbb{C}_2$ at point B, respectively. The notation $(\dot{})$ denotes a derivative with respect to time.

The rolling conditions for the pin on curves $\mathbb{C}_1$ and $\mathbb{C}_2$ are

$$\dot{s}_1 = \frac{1}{2}\,d\dot{\theta}; \quad \dot{s}_2 = \frac{1}{2}\,d\dot{\gamma}, \tag{4}$$

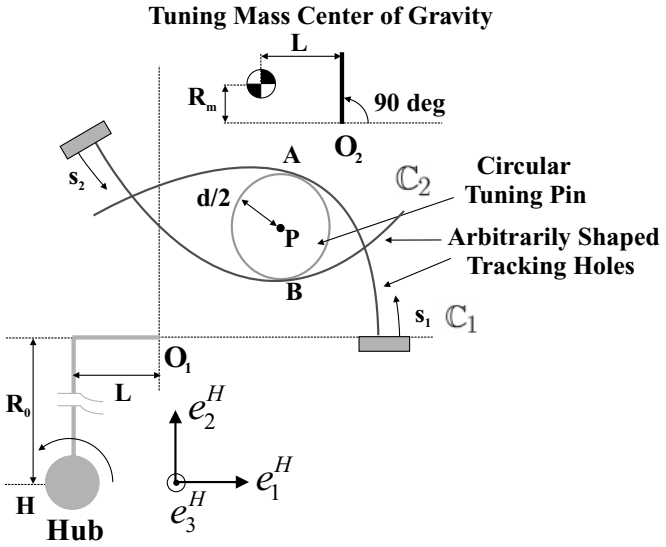

Fig. 5. Configuration of the bifilar pendulum with arbitrarily shaped tracking holes.

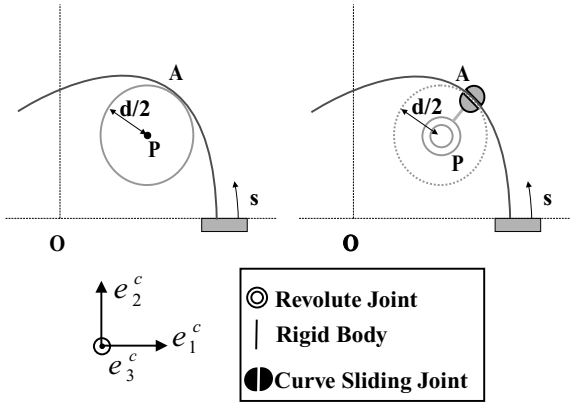

Fig. 6. Rolling pin on an arbitrarily shaped curve.

respectively. These constraints are enforced as nonholonomic constraints of the form

$$\mathcal{C}_1 = \dot{s}_1 - \frac{1}{2}\,d\dot{\theta}; \quad \mathcal{C}_2 = \dot{s}_2 - \frac{1}{2}\,d\dot{\gamma}. \tag{5}$$

Details of the formulation of the constraint forces and their discretization for nonholonomic constraints can be found in Ref. 25.

Multibody representation

In order to ease the understanding of the bifilar multibody formulation, consider first the rolling pin shown in Fig. 6. An orthonormal basis $\mathcal{S}^C := (\mathbf{e}_1^C, \mathbf{e}_2^C, \mathbf{e}_3^C)$ is attached at point O. A rolling pin of diameter d is in contact with a curve of arbitrary shape at point A. The angular velocity of the pin measured in the Frenet triad associated with the curve at point A is denoted by $\underline{\omega}^* = -\dot{\theta}\,\underline{e}_3^C$. The rolling condition is then $\dot{s} = d/2\,\dot{\theta}$.

This system can be modeled with a multibody formulation. A curve sliding joint connects the curve to a rigid body of length $d/2$. This rigid body is attached to a revolute joint whose relative rotation defines the pin's angular motion θ measured in the Frenet triad of the curve at the

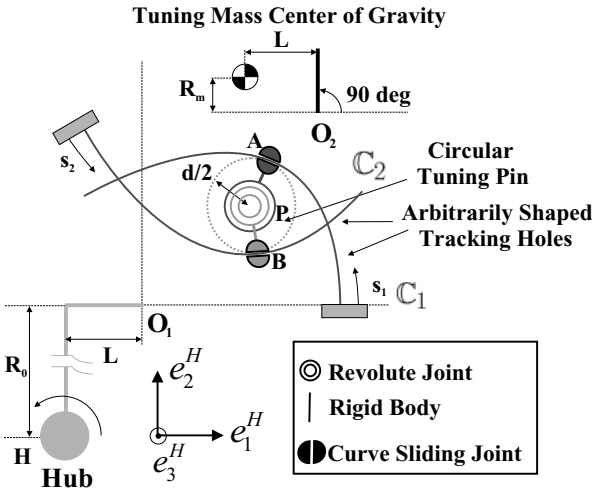

Fig. 7. Multibody representation of the bifilar pendulum with arbitrarily shaped tracking holes.

contact point. By enforcing the nonholonomic constraint $\mathcal{C} = \dot{s} - d/2\,\dot{\theta}$, this multibody system becomes kinematically equivalent to a pin rolling on a curve of arbitrary shape. The system will also be dynamically equivalent provided that inertia properties of the pin are associated to the inner race of the revolute joint.

Consider now the multibody model of the bifilar pendulum shown in Fig. 7. In essence, the bifilar pendulum consists of two interconnected fictitious pins rolling on curves of arbitrary shape. First, a curve sliding joint connects a rigid body of length $d/2$ to curve $\mathbb{C}_1$. This rigid body is attached to a revolute joint whose relative rotation defines the pin angular motion θ and its time derivative $\dot{\theta}$, both measured in the Frenet triad of the curve $\mathbb{C}_1$ at the contact point. This assembly defines the first fictitious pin.

Next, a second curve sliding joint joins a rigid body of length $d/2$ to curve $\mathbb{C}_2$. This rigid body is connected to a revolute joint whose relative rotation defines the pin's angular motion γ and its time derivative $\dot{\gamma}$, both measured in the Frenet triad associated with $\mathbb{C}_2$ at the contact point. This assembly defines the second fictitious pin. Finally, the two fictitious pins are connected to each other at point P, i.e., the inner races of the revolute joints that define θ and γ are attached to each other and define the tuning pin. By associating the mass properties of the tuning pin with the inner race of the revolute joint, a dynamically equivalent multibody representation is achieved.

Dynamic Analysis

Consider first a bifilar pendulum with circular tracking holes of identical diameter D. The hub rotates at constant angular speed Ω. It is then easy to show that the linearized equation of motion of the system becomes

$$\Delta\ddot{\phi} + \omega^2\,\Delta\phi = 0, \tag{6}$$

where $\Delta\phi$ is a small angular motion of the tuning mass. The natural frequency of the system, ω, is given by

$$\omega^2 = \Omega^2 \left[\frac{m_b + m_p \dfrac{R_0}{R}}{m_b + \dfrac{m_p}{2} + \dfrac{2I_p}{d^2}} \right] \frac{R}{D-d}, \tag{7}$$

where $R = R_0 + R_m$; m_p, m_b are the masses of the pin and tuning mass, respectively; and I_p is the pin's polar moment of inertia. In Sikorsky's UH-60, the bifilar pendulum is tuned to a frequency $\omega = 3P$ such that it will absorb the in-plane hub vibration corresponding to a $3P$ excitation in the rotating frame. The $3P$ and $5P$ harmonics in the rotating system both contribute to the $4P$ excitation in the fixed system.

The bifilar pendulum with circular tracking holes of equal diameter is equivalent to a simple pendulum. As the amplitude of vibration of the tuning mass increases, the natural frequency of the system changes. In fact, the period T of vibration of a simple pendulum of length ℓ under gravity g as a function of initial amplitude θ_0 is given by a complete elliptic integral of the form (Ref. 26)

$$T = \frac{4}{\omega} \int_0^{\pi/2} \frac{\mathrm{d}\psi}{\sqrt{1 - k^2 \sin\psi}}, \tag{8}$$

where $\omega = \sqrt{g/\ell}$ and $k = \sin\theta_0/2$. For small amplitude vibrations, the period becomes $T = 2\pi/\omega$, and is independent of initial amplitude. As the amplitude of vibration increases, the period increases, the pendulum is no longer tuned to the desired $3P$ frequency, and the effectiveness of the device as a vibration absorber decreases. Consequently, the bifilar pendulum used in the UH-60 features tracking holes of cycloidal shape for which the period of the bifilar becomes nearly independent of amplitude.

Formulation of the Curve Sliding Joint

Consider two bodies denoted with superscripts $(.)^k$ and $(.)^\ell$, respectively, linked together by a curve sliding joint as shown in Fig. 8. Body k is a rigid body whose external shape is described by a spatial curve $\mathbb{C}$. The orientation of this body is defined by orthonormal bases $\mathcal{S}^{0k} := (\mathbf{e}_{01}^k, \mathbf{e}_{02}^k, \mathbf{e}_{03}^k)$ and $\mathcal{S}^k := (\mathbf{e}_1^k, \mathbf{e}_2^k, \mathbf{e}_3^k)$ in the reference and deformed configurations, respectively. Similarly, two additional orthonormal bases define the orientation of body ℓ, $\mathcal{S}^{0\ell} := (\mathbf{e}_{01}^\ell, \mathbf{e}_{02}^\ell, \mathbf{e}_{03}^\ell)$ and $\mathcal{S}^\ell := (\mathbf{e}_1^\ell, \mathbf{e}_2^\ell, \mathbf{e}_3^\ell)$ in the reference and deformed configurations, respectively. R_0^k and R^k are the components of the rotation tensors from $\mathcal{S}^I$ to $\mathcal{S}^{0k}$ and $\mathcal{S}^{0k}$ to $\mathcal{S}^k$, respectively, both measured in $\mathcal{S}^I$. Similarly, R_0^ℓ and R^ℓ are the components of the rotation tensors from $\mathcal{S}^I$ to $\mathcal{S}^{0\ell}$ and $\mathcal{S}^{0\ell}$ to $\mathcal{S}^\ell$, respectively, both measured in $\mathcal{S}^I$.

A curve sliding joint involves displacement constraints; optionally, rotation constraints might be added. The displacement constraints imply that a point of body ℓ must be in contact with curve $\mathbb{C}$ at all times. The

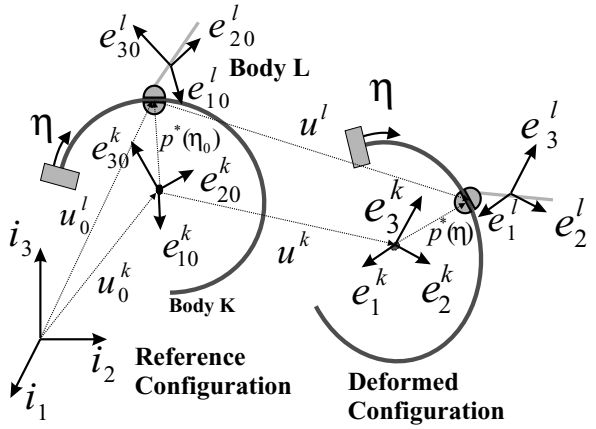

Fig. 8. Configuration of the curve sliding joint: Displacement constraints.

rotation constraints imply that the orientation of body ℓ with respect to the Frenet triad of the curve at the contact point must remain constant at all times.

Displacement constraints

Let $\underline{p}^*(\eta)$ be the components of the position vector of a point on curve $\mathbb{C}$ measured in $\mathcal{S}^k$, and $\underline{P}^k$ those of the position vector of an arbitrary point on curve $\mathbb{C}$, measured in $\mathcal{S}^I$. It then follows that

$$\underline{P}^k = \underline{u}_0^k + \underline{u}^k + R^k R_0^k \, \underline{p}^*(\eta). \tag{9}$$

Similarly, the components of the position vector of the point of body ℓ in contact with the curve, measured in $\mathcal{S}^I$, are

$$\underline{P}^\ell = \underline{u}_0^\ell + \underline{u}^\ell. \tag{10}$$

Since bodies k and ℓ must remain in contact, the following vector constraint must be satisfied

$$\underline{\mathcal{C}} = \underline{P}^k - \underline{P}^\ell = \underline{u}_0 + \underline{u} + R^k R_0^k \, \underline{p}^*(\eta) = \underline{0}, \tag{11}$$

where $\underline{u}_0 = \underline{u}_0^k - \underline{u}_0^\ell$ and $\underline{u} = \underline{u}^k - \underline{u}^\ell$. These nonlinear holonomic constraints are enforced by the addition of a constraint potential $\underline{\lambda}^T \underline{\mathcal{C}}$, where $\underline{\lambda}$ is a set of Lagrange multiplier. The forces of constraint $\underline{\mathcal{F}}^c$ corresponding to this constraint are readily obtained as

$$\underline{\lambda}^T \, \delta\underline{\mathcal{C}} = \begin{bmatrix} \delta\underline{u}^k \\ \delta\underline{\psi}^k \\ \delta\underline{u}^\ell \\ \delta\eta \end{bmatrix}^T \begin{bmatrix} \underline{\lambda} \\ -\left[R^k R_0^k \, \underline{p}^*(\eta)\right]^{\sim} \underline{\lambda} \\ -\underline{\lambda} \\ \left[R^k R_0^k \, \underline{p}^{*'}(\eta)\right]^T \underline{\lambda} \end{bmatrix} = \begin{bmatrix} \delta\underline{u}^k \\ \delta\underline{\psi}^k \\ \delta\underline{u}^\ell \\ \delta\eta \end{bmatrix}^T \underline{\mathcal{F}}^c, \tag{12}$$

where $(.)' = \mathrm{d}(.)/\mathrm{d}\eta$ and $\widetilde{\delta\psi}^k = \delta R^k R^{kT}$ is the virtual rotation vector. Details of the discretization of the constraint forces can be found in Refs. 23 and 24.

Rotation constraints

The rotation constraints associated with the curve sliding joint imply that the orientation of body ℓ with respect to the Frenet triad of the curve at the contact point must remain constant at all times. This constraint is necessary for modeling the bifilar pendulum, as explained in earlier sections. Figure 9 shows bodies k and ℓ connected by means of a curve sliding joint. Let $\underline{t}^*(\eta)$, $\underline{n}^*(\eta)$ and $\underline{b}^*(\eta)$ be the components of the unit tangent, normal and binormal vectors to the curve, measured in $\mathcal{S}^k$, respectively. For convenience, the following rotation tensor is defined

$$R^*(\eta) = [\underline{t}^*(\eta), \underline{n}^*(\eta), \underline{b}^*(\eta)]. \tag{13}$$

The unit tangent vector to the curve at the contact point in the reference configuration, measured in $\mathcal{S}^k$, can now be written as $\underline{t}_0^* = R^*(\eta_0) \, \underline{i}_1^*$, where $\underline{i}_1^{*T} = \lfloor 1 \; 0 \; 0 \rfloor$, and η_0 denotes the position of the contact point in the reference configuration. Expressing this vector in the global frame $\mathcal{S}^I$ leads to

$$\underline{t}_0 = R_0^k \, \underline{t}_0^* = R_0^k R^*(\eta_0) \, \underline{i}_1^*. \tag{14}$$

Similarly, the unit tangent to the curve at the contact point in the deformed configuration, measured in $\mathcal{S}^k$, is $\underline{t}^* = R^*(\eta) \, \underline{i}_1^*$. The components of this

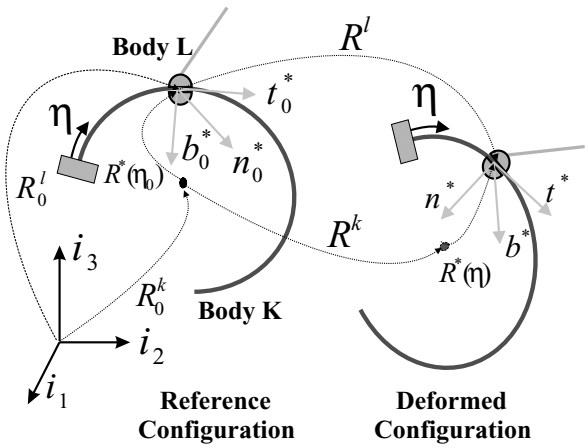

Fig. 9. Configuration of the curve sliding joint: Rotation constraints.

vector in the global frame $\mathcal{S}^I$ are now

$$\underline{t} = R^k R_0^k \, \underline{t}^* = R^k R_0^k R^*(\eta) \, \underline{i}_1^*. \tag{15}$$

Combining Eqs. (15) and (14) then yields a relationship between the orientations of the unit tangent vectors in the reference and deformed configurations:

$$\underline{t} = R^k R_0^k R^*(\eta) R^{*T}(\eta_0) R_0^{kT} \, \underline{t}_0. \tag{16}$$

Consequently, the finite rotation tensor $R^k R_0^k R^*(\eta) R^{*T}(\eta_0) R_0^{kT}$ represents the rotation of the Frenet triad from the reference to the deformed configuration, measured in $\mathcal{S}^I$. As expected, this finite rotation depends on the location of the point of contact in the reference and deformed configurations through the rotation tensors $R^{*T}(\eta_0)$ and $R^*(\eta)$; it also depends on the rotation of body k through rotation tensor R^k, and on its initial orientation through R_0.

A similar relationship can be derived for body ℓ

$$\underline{e}_1^\ell = R^\ell \, \underline{e}_{01}^\ell. \tag{17}$$

Consequently, the finite rotation tensor R^ℓ represents the rotation of body ℓ from the reference to the deformed configuration, measured in $\mathcal{S}^I$. The rotation constraints associated with the curve sliding joint enforces the orientation of body ℓ with respect to the Frenet triad of the curve at the contact point to remain constant at all times. This clearly implies

$$R^\ell = R^k R_0^k R^*(\eta) R^{*T}(\eta_0) R_0^{kT}. \tag{18}$$

This constraint can be rewritten as $R^\ell R_0^k R^*(\eta_0) R^{*T}(\eta) R_0^{kT} R^{kT} = I$, where I is the identity tensor. For convenience, this constraint is expressed in $\mathcal{S}^k$ as

$$\bar{R} = R^{*T}(\eta) R_0^{kT} R^{kT} R^\ell R_0^k R^*(\eta_0) = I. \tag{19}$$

Since $\bar{R}$ is an orthogonal tensor, this constraint corresponds to three independent scalar constraints only

$$\begin{bmatrix} \bar{R}_{32} - \bar{R}_{23} \\ \bar{R}_{13} - \bar{R}_{31} \\ \bar{R}_{21} - \bar{R}_{12} \end{bmatrix} = \underline{0}. \tag{20}$$

For convenience, the following vectors are defined

$$\underline{j}_\alpha^k = R^k R_0^k R^*(\eta) \, \underline{i}_\alpha; \quad \underline{j}_\alpha^\ell = R^\ell R_0^k R^*(\eta_0) \, \underline{i}_\alpha, \quad \alpha = 1, 2, 3. \tag{21}$$

and Eq. (20) becomes

$$\begin{bmatrix} \underline{j}_3^{kT}\,\underline{j}_2^{\ell} - \underline{j}_2^{kT}\,\underline{j}_3^{\ell} \\ \underline{j}_1^{kT}\,\underline{j}_3^{\ell} - \underline{j}_3^{kT}\,\underline{j}_1^{\ell} \\ \underline{j}_2^{kT}\,\underline{j}_1^{\ell} - \underline{j}_1^{kT}\,\underline{j}_2^{\ell} \end{bmatrix} = \underline{0}. \tag{22}$$

These three scalar constraints correspond to constraining the relative rotation of body ℓ with respect to the Frenet triad about the local tangent, normal, and binormal directions, respectively. These nonlinear holonomic constraints each are of the form

$$\mathcal{C} = \underline{j}_\alpha^{kT}\,\underline{j}_\beta^{\ell} - \underline{j}_\beta^{kT}\,\underline{j}_\alpha^{\ell}; \quad \alpha \neq \beta. \tag{23}$$

The forces of constraint $\underline{\mathcal{F}}^c$ corresponding to this constraint are readily obtained as

$$\lambda\,\delta\mathcal{C} = \begin{bmatrix} \underline{\delta\psi}^k \\ \underline{\delta\psi}^{\ell} \\ \delta\eta \end{bmatrix}^T \begin{bmatrix} \lambda\left(\widetilde{j}_\alpha^k\,\underline{j}_\beta^{\ell} - \widetilde{j}_\beta^k\,\underline{j}_\alpha^{\ell}\right) \\ -\lambda\left(\widetilde{j}_\alpha^k\,\underline{j}_\beta^{\ell} - \widetilde{j}_\beta^k\,\underline{j}_\alpha^{\ell}\right) \\ \lambda\left(\underline{j}_\beta^{lT}\,\underline{j}_\alpha^{k\prime} - \underline{j}_\alpha^{lT}\,\underline{j}_\beta^{k\prime}\right) \end{bmatrix} = \begin{bmatrix} \underline{\delta\psi}^k \\ \underline{\delta\psi}^{\ell} \\ \delta\eta \end{bmatrix}^T \underline{\mathcal{F}}^c, \tag{24}$$

where $\widetilde{\delta\psi}^k = \delta R^k R^{kT}$ and $\widetilde{\delta\psi}^{\ell} = \delta R^{\ell} R^{\ell T}$ are the virtual rotation vector for body k and ℓ, respectively; $\underline{j}_\alpha^{k\prime} = R^k R_0^k R^{*\prime}(\eta)\,\underline{i}_\alpha$; and $\underline{j}_\beta^{k\prime} = R^k R_0^k R^{*\prime}(\eta)\,\underline{i}_\beta$. The notation $(.)'$ is used to denote a derivative with respect to η. Details of the discretization of the constraint forces can be found in Refs. 23 and 24.

The rolling constraints shown in Eq. (5) were written in terms of the curvilinear coordinates s_1 and s_2 of the corresponding curves. However, the NURBS representation of curves (Refs. 20, 21) makes use of the nondimensional parameter $\eta \in [0, 1]$ to parameterize curves. Consequently, an additional scalar constraint relating these variables is necessary. This constraint is easily cast as a nonlinear, nonholonomic constraint

$$\mathcal{C} = \dot{s} - |\underline{p}^{*\prime}(\eta)|\,\dot{\eta} = 0. \tag{25}$$

Numerical Examples

Validation example

As a validation example, consider the system depicted in Fig. 10. A small collar of mass m slides without friction under the effect of gravity g on two different curves: a circle and a cycloid. The circle is of radius R and the cycloid is described by the function $\underline{p}(t) = a(t + \sin t)\,\underline{i}_1 - a(1 + \cos t)\,\underline{i}_2$, where a is a constant and $t \in [-\pi, \pi]$ is the curve parameter. The collar position is described by angle θ defined in Fig. 10. The collar is initially at rest with an angular position θ_0. The system was modeled using a curve sliding joint that connected the collar to the curve.

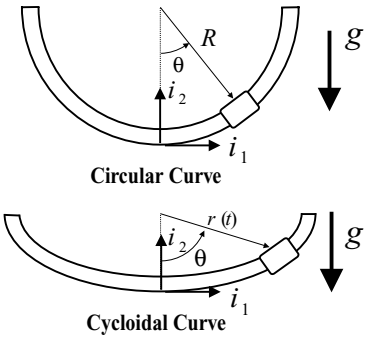

Fig. 10. Validation example for circular and cycloidal curves.

The physical properties of the system are as follows: collar mass $m = 2.0$ kg, radius $R = 1.0$ m, cycloid constant $a = 0.25$ m, and acceleration of gravity $g = 9.81$ m/sec^2. Two cases were considered for each curve, denoted *case 1* and *2*, corresponding to collar polar moments of inertia $I_p = 0$ and 0.25 kg $\cdot$ m^2, respectively. In *case 2*, the collar is no longer a point mass; the rotation constraint associated with the curve sliding joint impart an angular velocity to the collar as it slides along the curve and an additional kinetic energy component arises. For *case 1*, the period of oscillation T for the collar sliding on the circle is a function of initial amplitude θ_0 given by Eq. (8) with $\omega = \sqrt{g/R}$. On the other hand, the period of oscillation for the cycloid is a constant (Ref. 26)

$$T = 4\,\pi\sqrt{\frac{a}{g}}. \tag{26}$$

Figure 11 compares the analytical and numerical results. Excellent agreement between analytical and numerical results is observed for both circular and cycloidal curves.

For *case 2*, the period of oscillation for the collar on the circle is given by Eq. (8) with $\omega = \sqrt{(1 + \rho^2/R^2)\,g/R}$, where ρ is the radius of gyration of the collar. The period of oscillation of a point mass on a cycloid was found to be

$$T = 4\sqrt{\frac{2a}{g}}\int_0^1 \sqrt{\frac{\frac{1}{2} + \frac{1}{16}\left(\frac{\rho}{a}\right)^2 \frac{1}{2 - (y_0/a)u}}{u - u^2}}\,\mathrm{du}, \tag{27}$$

where y_0 is the initial vertical position of the collar. Figure 12 compares the analytical and numerical predictions; excellent correlation is found. Clearly, the period of oscillation for the cycloid is dependent on the initial position of the collar, however, for $\theta_0 \leq 50$ deg, it remains nearly constant.

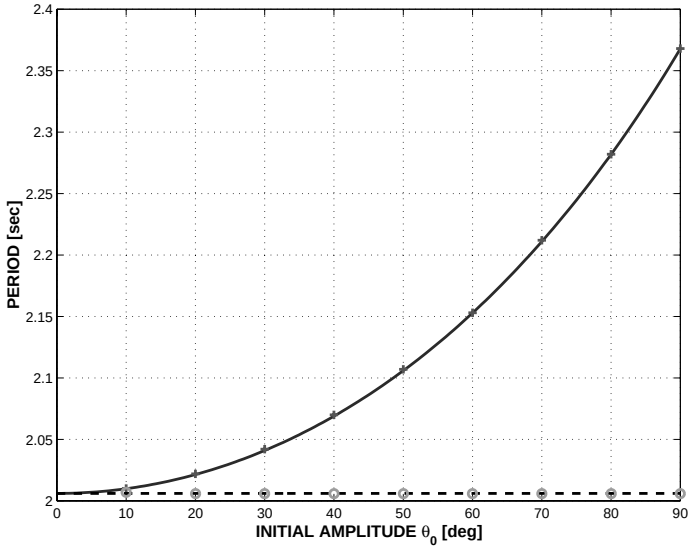

Fig. 11. Periods of oscillation for a point mass (*case 1*) on a circle: analytical results, Eq. (8), solid line; numerical results, (+). Periods of oscillation for a point mass (*case 1*) on a cycloid: analytical results, Eq. (26), dashed line; numerical results, (○).

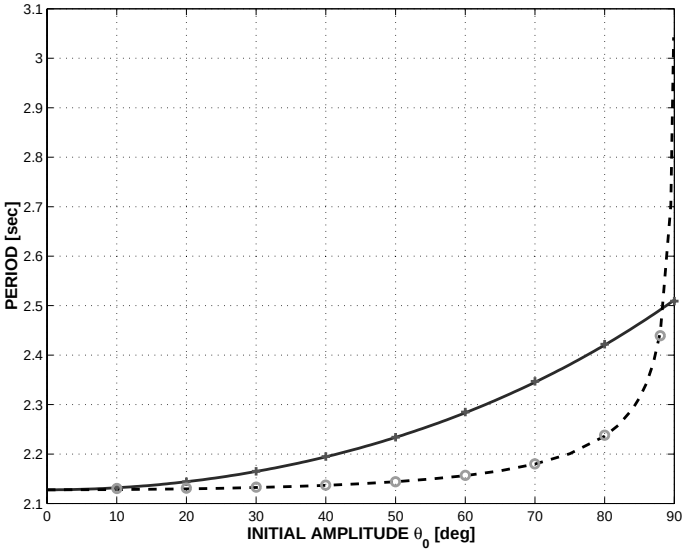

Fig. 12. Periods of oscillation for a body (*case 2*) on a circle: analytical results, Eq. (8), solid line; numerical results, (+). Periods of oscillation for a body (*case 2*) on a cycloid: analytical results, Eq. (27), dashed line; numerical results, (○).

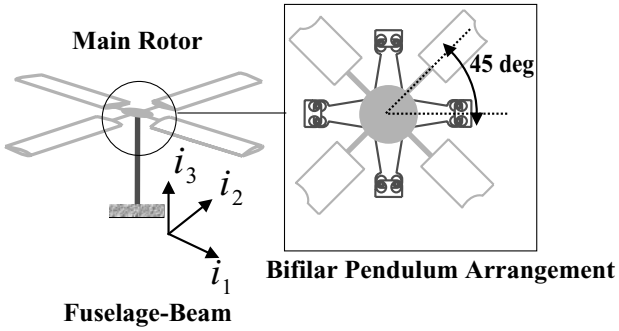

Fig. 13. Arrangement of the bifilar pendulums on a four-bladed rotor.

Four bladed rotor analysis

Next, a practical example is described: Sikorsky's UH-60 helicopter with hub mounted bifilar pendulums. The UH-60 is a four-bladed helicopter whose physical properties are described in Ref. 27 and references therein. Figure 13 shows the helicopter configuration used in the present simulation. The main rotor is connected to a nonrotating beam clamped to the ground that models the elasticity of the fuselage and shaft. This beam will be denoted the fuselage-beam. Four bifilar pendulums are rigidly connected to the hub. Each bifilar pendulum makes a 45 deg angle with respect to the nearest blade. A detailed description of the physical properties of the bifilar pendulum used in the present analysis can be found in Refs. 2 and 4. Each blade was modeled using six cubic beam elements, and the flap, lag, and pitching hinges by revolute joints. Each bifilar pendulum was modeled with a combination of revolute, curve sliding, and planar joints, as described in earlier sections. The aerodynamic forces acting on the system were computed based on the unsteady, two-dimensional airfoil theory developed by Peters et al. (Ref. 28), and the three-dimensional unsteady inflow model developed by Peters and He (Ref. 29). During the simulation, the control inputs were set to the following values, termed standard control inputs: collective $\theta_0 = 10.7$ deg, longitudinal cyclic $\theta_s = -4.9$ deg, lateral cyclic $\theta_c = 4.7$ deg. The helicopter was in a forward flight at a speed of $U = 150$ ft/sec.

Table 1. Description of the various cases

Case Number	Bifilar Behavior	Bifilar Frequency	Fuselage-Beam Stiffness
0	Locked	N/A	Nominal
1	Free	3P	Nominal
2	Free	3.3P	Nominal
3	Free	3P	0.5 × nominal

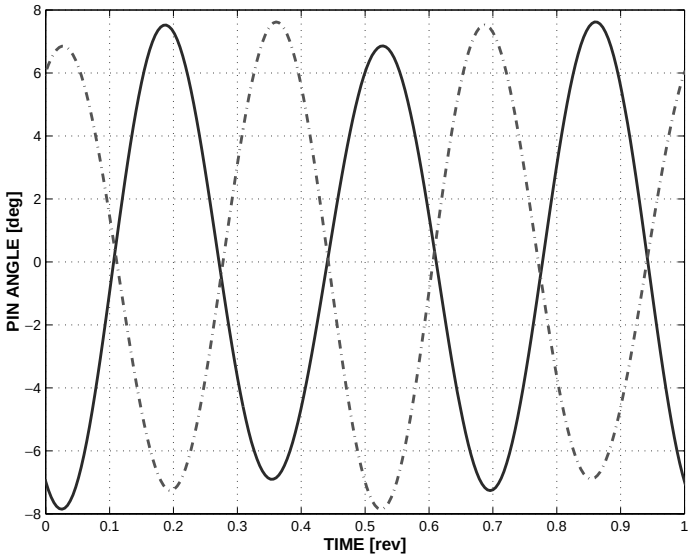

Fig. 14. Time history of the pin angles for *case 1*: pin *A* solid line; pin *B* (180 degrees apart) dashed-dotted line.

Three cases, denoted *case 0* through *2* were considered. *Case 0* is the baseline case. The bifilars were mounted on the hub, however, the relative motion of the each bifilar mass with respect to the hub frame was prevented. In *case 1*, the bifilar mass was allowed to move and the pendulum was tuned to a frequency of $3P$. *Case 2* is identical to *case 1* except that frequency of the bifilar pendulum was increased by 10%. Table 1 summarizes the various cases studied in this example. The simulations were run for several main rotor revolutions until a periodic solution was reached. The figures presented below show the response of the rotor for one period, once the periodic solution is achieved.

Figure 14 shows the pin angle ϕ for two bifilar pendulums separated by 180 deg. The pin angle ϕ is defined as follows: a straight line connecting the center of the circular pin to the center of its tracking hole makes an angle ϕ with the bifilar's support arm, see Fig. 1. Clearly, the pin angle responses for the two bifilar pendulums are 180 deg out-of-phase, reaching a maximum amplitude of 7 deg. Each pin response is at a $3P$ frequency, as expected. Obviously, the pin angles for *case 0* are zero. Figure 15 depicts the motion of the hub in the rotor plane and the motion of the center of mass of the four bifilars tuning masses for *cases 0* and *1*. In *case 0*, since the tuning masses are locked in place, the motion of their center of mass is identical to that of the hub. Clearly, there is a significant reduction in hub displacement amplitude when comparing *cases 0* and *1*, indicating that the bifilar pendulums are quite effective.

As mentioned earlier, the bifilar pendulums are tuned at a $3P$ frequency in order to absorb in-plane hub vibrations resulting from a $3P$ excitation in the rotating frame. The $3P$ and $5P$ harmonics in the rotating

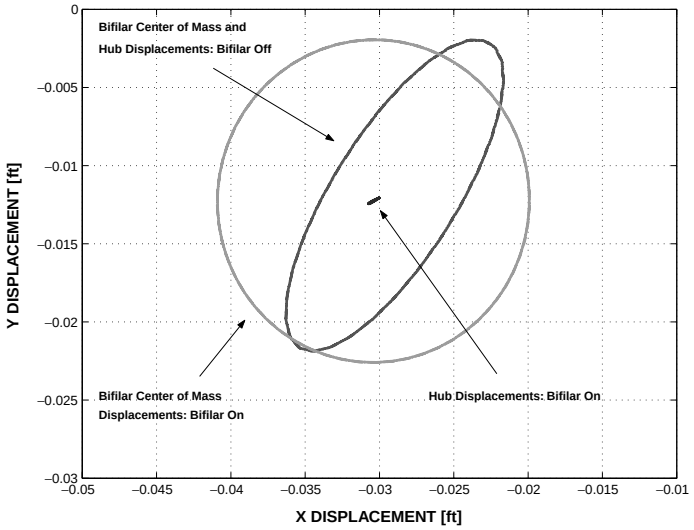

Fig. 15. In-plane hub and bifilar center of mass displacements for *cases 0* (bifilar off) and *1* (bifilar on).

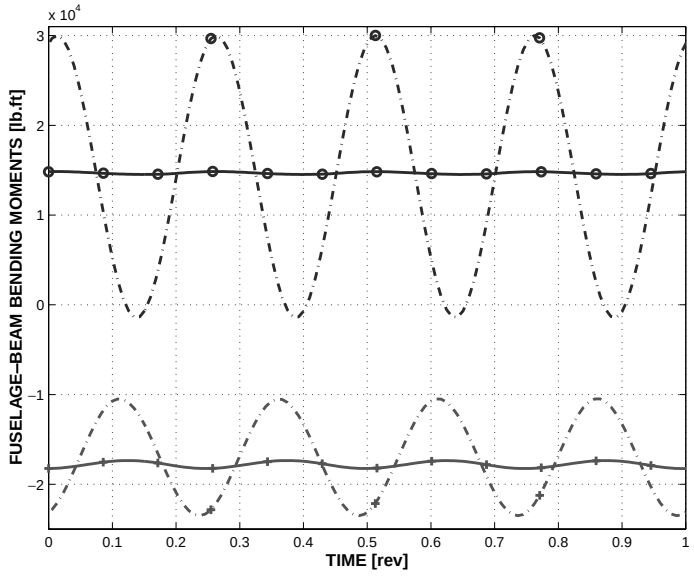

Fig. 16. Time history of the fuselage-beam root bending moments in the fixed system, M_{11}, (○), and M_{22}, (+). *Case 0*: dashed-dotted line; *case 1*: solid line.

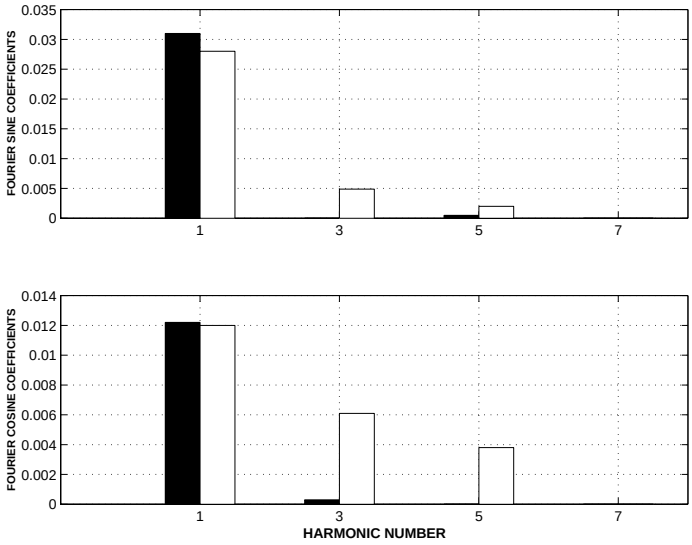

Fig. 17. Fourier harmonics of the inertial hub displacements expressed in the rotating frame for *case 0*: white bars and *case 1*: black bars.

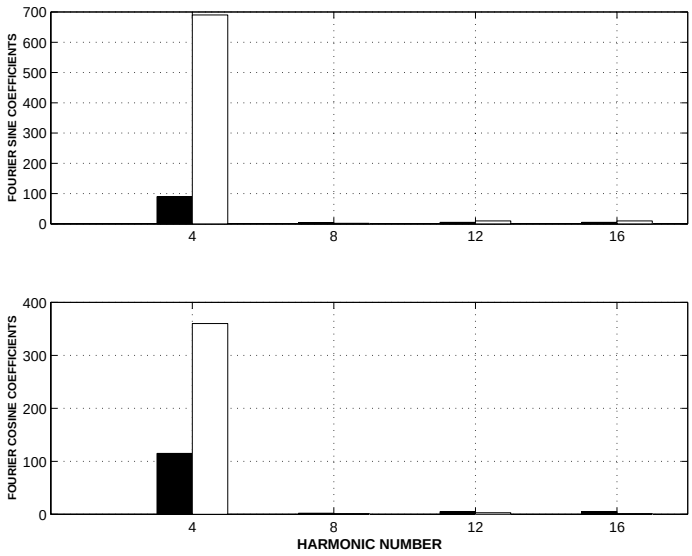

Fig. 18. Fourier harmonics of the hub in-plane forces expressed in the fixed system for *case 1*: black bars and *case 2*: white bars.

system contribute to the $4P$ excitation in the fixed system. When the bifilars are active, the center of mass of their tuning masses describes a circular path that completes four revolutions per main rotor revolution, i.e., the fixed system response is at a $4P$ frequency. In essence, the bifilar pendulums act as simple vibration absorbers. Due to the motion of their center of mass, a force is applied on the hub at the excitation frequency but out-of-phase with the excitation forces. Consequently, hub displacements are small compared to those of the center of mass of the four bifilars, as observed from Fig. 15. Figure 16 depicts the fuselage-beam root bending moments in the fixed system for *cases 0* and *1*. In the caption of these figures, M_{11} and M_{22} are root bending moment in fuselage x and y directions respectively. As expected, the response is at a $4P$ frequency. The effectiveness of the bifilar pendulums is clearly demonstrated: the amplitude of the response is reduced drastically from *case 0* to *case 1*.

Figure 17 shows the Fourier harmonics of the inertial hub displacements expressed in the rotating frame, for *cases 0* and *1*. As expected, the bifilar pendulums reduce the $3P$ response almost completely. Figure 18 depicts the Fourier harmonics of the hub in-plane forces which include both contributions from rotor and bifilar expressed in the fixed system, for *cases 1* and *2*. *Case 1* corresponds to the "tuned bifilar" (tuned to the $3P$ frequency), whereas *case 2* is the "detuned bifilar" case (10% above the $3P$ frequency). Clearly, detuning drastically degrades bifilar performance and hence, it is important to use cycloidal shaped tracking holes to keep the pendulum tuned at all amplitudes.

The proposed multibody formulation provides a rigorous model of the bifilar pendulum. Present industry practice is to replace the bifilar pendulum by an equivalent, single degree of freedom oscillator in the fixed system. Such models are inherently linearized approximations of the bifilar dynamic behavior and cannot capture the effects associated

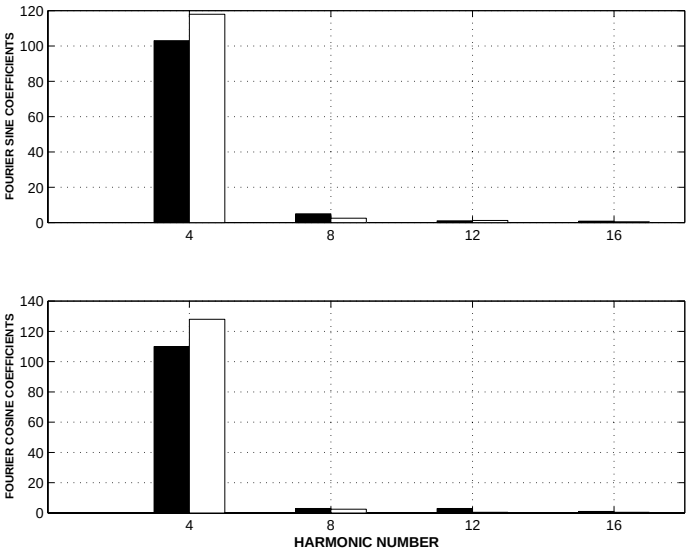

Fig. 19. Fourier harmonics of the hub in-plane forces expressed in the fixed system for *case 1*: black bars and *case 3*: white bars.

with tracking holes of arbitrary shape. The present simulation is of a qualitative, not quantitative nature: several aspects of the model must be improved to obtain accurate predictions. First, a more sophisticated aerodynamic model should be used. Similarly, the structural dynamics model was simplified: control linkages such as the pitchlinks and swashplates were not modeled. Finally, the fuselage-beam model is a very crude approximation to the fuselage dynamic behavior: fuselage inertia properties were not taken into account and its stiffness characteristics were greatly simplified. Figure 19 shows the Fourier harmonics of the hub in-plane forces expressed in the fixed system, for *cases 1* and *3*. *Case 1* corresponds to the baseline case and *case 3* is identical to *case 1* except for the fuselage-beam bending stiffness EI_{33} that was reduced by a factor of two, see Table 1. Clearly, there are significant differences between both cases: the in-plane force harmonics are increased by 20% from *case 1* to *3*. This points out the need for an accurate model of the elastic and inertial characteristics of the fuselage for accurate hub load predictions.

Conclusions

A model of the bifilar pendulum has been presented within the framework of flexible, nonlinear multibody dynamics. A detailed model of the system involved a series of nonlinear holonomic and nonholonomic constraints. This work was developed within the framework of energy preserving and decaying time integration schemes that provide unconditional stability for nonlinear, flexible multibody systems.

The proposed formulation required the development of a curve sliding joint, that seems, at first sight, unrelated to a bifilar pendulum. However, it was shown that the curve sliding joint combined with other joints, such as the revolute joint, provides an effective modeling tool for the bifilar pendulum. This approach, the combination of a number of basic kinematic joints to construct realistic models of complex hardware components, provides a powerful tool for the detailed modeling of rotorcraft systems. The ability to model new configurations of arbitrary topology through the assembly of basic components chosen from an extensive library of elements is highly desirable. In fact, this approach is at the heart of the finite element method which has enjoyed, for this very reason, an explosive growth in the last few decades.

The present formulation results in a kinematically and dynamically exact model of the bifilar pendulum, under the assumption of rolling contact between the tuning pins and tracking holes. The formulation is valid for arbitrarily shaped tracking holes. The effectiveness of the bifilar pendulum for various shapes of the tracking hole could be investigated with the proposed formulation. The numerical examples presented in the paper demonstrated the validity of the proposed formulation from a qualitative standpoint: dramatic reduction in $3P$ vibration for a bifilar tuned at $3P$. Improvements in the aerodynamic, structural dynamics, and fuselage models are necessary to obtain accurate predictions of hub loads.

References

[1]Den Hartog, J. P., *Mechanical Vibrations*, Dover Publications, New York, 1985, pp. 220–223.

[2]Miao, W., and Mouzakis, T., "Bifilar Analysis," NASA CR 159227, 1980.

[3]Mouzakis, T., "Monofilar, a Dual Frequency Rotorhead Absorber," American Helicopter Society Northeast Region National Specialists Meeting on Helicopter Vibration, Hartford, CT, November 1981, pp. 278–287.

[4]Sopher, R., Studwell, R. E., Cassarino, S., and Kottapalli, S. B. R., "Coupled Rotor/Airframe Vibration Analysis," NASA CR 3582, 1982.

[5]Nikravesh, P. E., *Computer-Aided Analysis of Mechanical Systems*, Prentice-Hall, Englewood Cliffs, NJ, 1988, Ch. 2.

[6]Géradin, M., and Cardona, A., *Flexible Multibody System: A Finite Element Approach*, John Wiley & Sons, New York, 2000, Ch. 1.

[7]Bauchau, O. A., Bottasso, C. L., and Nikishkov, Y. G., "Modeling Rotorcraft Dynamics with Finite Element Multibody Procedures," *Mathematical and Computer Modeling*, Vol. 33, 2001, pp. 1113–1137.

[8]Pfeiffer, F., and Glocker, C., *Multi-Body Dynamics with Unilateral Contacts*, John Wiley & Sons, New York, 1996, Ch. 4.

[9]Khulief, Y. A., and Shabana, A. A., "A Continuous Force Model for the Impact Analysis of Flexible Multi-Body Systems," *Mechanism and Machine Theory*, Vol. 22, 1987, pp. 213–224.

[10]Lankarani, H. M., and Nikravesh, P. E., "A Contact Force Model with Hysteresis Damping for Impact Analysis of Multi-Body Systems," *Journal of Mechanical Design*, Vol. 112, 1990, pp. 369–376.

[11]Cardona, A., and Géradin, M., "Kinematic and Dynamic Analysis of Mechanisms with Cams," *Computer Methods in Applied Mechanics and Engineering*, Vol. 103, 1983, pp. 115–134.

[12]Bauchau, O. A., "Analysis of Flexible Multi-Body Systems with Intermittent Contacts," *Multibody System Dynamics*, Vol. 4, 2000, pp. 23–54.

[13]Bauchau, O. A., "On the Modeling of Friction and Rolling in Flexible Multi-Body Systems," *Multibody System Dynamics*, Vol. 3, 1999, pp. 209–239.

[14]Bottasso, C. L., and Bauchau, O. A., "Multibody Modeling of Engage and Disengage Operations of Helicopter Rotors," *Journal of the American Helicopter Society*, Vol. 46, (4), October 2001, pp. 290–300.

[15]Bauchau, O. A., Rodriguez, J., and Bottasso, C. L., "Modeling of Unilateral Contact Conditions with Application to Aerospace Systems Involving Backlash, Freeplay and Friction," *Mechanics Research Communications*, Vol. 28, (5), 2001, pp. 571–599.

[16]Li, D., and Likins, P. W., "Dynamics of a Multibody System with Relative Translation on Curved, Flexible Tracks," *Journal of Guidance, Control, and Dynamics*, Vol. 10, 1987, pp. 299–306.

[17]Cardona, A., "An Integrated Approach to Mechanism Analysis," Ph.D. Dissertation, Université de Liège, 1989.

[18]Bauchau, O. A., "On the Modeling of Prismatic Joints in Flexible Multi-Body Systems," *Computer Methods in Applied Mechanics and Engineering*, Vol. 181, 2000, pp. 87–105.

[19]Bauchau, O. A., and Bottasso, C. L., "Contact Conditions for Cylindrical, Prismatic, and Screw Joints in Flexible Multi-Body Systems," *Multibody System Dynamics*, Vol. 5, 2001, pp. 251–278.

[20]Piegl, L., and Tiller, W., *The Nurbs Book*, Springer-Verlag, Berlin, 1997, Ch. 4.

[21]Farin, G. E., *Curves and Surfaces for Computer Aided Geometric Design*, Academic Press, Boston, MA, 1992, Ch. 6.

[22]Angeles, J., *Spatial Kinematic Chains*, Springer-Verlag, Berlin, 1982, Ch. 3.

[23]Bauchau, O. A., Bottasso, C. L., and Trainelli, L., "Robust Integration Schemes for Flexible Multibody Systems," *Computer Methods in Applied Mechanics and Engineering*, to appear.

[24]Bauchau, O. A., "Computational Schemes for Flexible, Nonlinear Multi-Body Systems," *Multibody System Dynamics*, Vol. 2, 1998, pp. 169–225.

[25]Bauchau, O. A., and Rodriguez, J., "Simulation of Wheels in Nonlinear, Flexible Multi-Body Systems," *Multibody System Dynamics*, Vol. 7, 2002, pp. 407–438.

[26]Webster, A. G., *Dynamics*, G. E. Stechert & CO., New York, 1942, pp. 322–325.

[27]Bousman, W. G., "An Investigation of Helicopter Rotor Blade Flap Vibratory Loads," American Helicopter Society 48th Annual Forum Proceedings, Washington, DC, June 3–5, 1992, pp. 977–999.

[28]Peters, D. A., Karunamoorthy, S., and Cao, W. M., "Finite State Induced Flow Models. Part I: Two-Dimensional Thin Airfoil," *Journal of Aircraft*, Vol. 32, 1985, pp. 313–322.

[29]Peters, D. A., and He, C. J., "Finite State Induced Flow Models. Part II: Three-Dimensional Rotor Disk," *Journal of Aircraft*, Vol. 32, 1985, pp. 323–333.